

RoboPol: AGN polarimetric monitoring data

D. Blinov^{1,2,3*}, S. Kiehlmann^{1,2}, V. Pavlidou^{1,2}, G. V. Panopoulou^{4†}, R. Skalidis^{1,2}, E. Angelakis⁵, C. Casadio^{1,2,6}, E. N. Einoder⁴, T. Hovatta^{7,8}, K. Kokolakis^{9,2}, A. Kougentakis¹, A. Kus¹⁰, N. Kylafis^{2,1}, E. Kyritsis^{2,1}, A. Lalakos¹¹, I. Liodakis⁷, S. Maharana¹², E. Makrydopoulou², N. Mandarakas^{1,2}, G. M. Maragkakis^{13,2}, I. Myserlis⁶, I. Papadakis^{1,2}, G. Paterakis¹, T. J. Pearson⁴, A. N. Ramaprakash^{12,1,4}, A. C. S. Readhead⁴, P. Reig^{2,1}, A. Słowikowska¹⁰, K. Tassis^{1,2}, K. Xexakis², M. Żejmo¹⁴, J. A. Zensus⁶

¹Institute of Astrophysics, Foundation for Research and Technology-Hellas, Voutes, 71110 Heraklion, Greece

²Department of Physics, University of Crete, 71003, Heraklion, Greece

³Astronomical Institute, St. Petersburg State University, Universitetsky pr. 28, Petrodvorets, 198504 St. Petersburg, Russia

⁴Cahill Center for Astronomy and Astrophysics, California Institute of Technology, 1200 E California Blvd, MC 350-17, Pasadena CA, 91125, USA

⁵Section of Astrophysics, Astronomy & Mechanics, Department of Physics, National and Kapodistrian University of Athens, Panepistimiopolis Zografos 15784, Greece

⁶Max-Planck-Institut für Radioastronomie, Auf dem Hügel 69, 53121 Bonn, Germany

⁷Finnish Centre for Astronomy with ESO, FINCA, University of Turku, Quantum, Vesilinnantie 5, FI-20014, Finland

⁸Aalto University Metsähovi Radio Observatory, Metsähovintie 114, FI-02540 Kylmälä, Finland

⁹Geodesy and Geomatics Engineering Laboratory, Technical University of Crete, GR-73100 Chania, Greece

¹⁰Institute of Astronomy, Faculty of Physics, Astronomy and Informatics, Nicolaus Copernicus University in Toruń, Grudziadzka 5, PL-87-100 Toruń, Poland

¹¹Center for Interdisciplinary Exploration & Research in Astrophysics (CIERA), Northwestern University, Evanston, IL 602, USA

¹²Inter-University Centre for Astronomy and Astrophysics, Post Bag 4, Ganeshkhind, Pune - 411 007, India

¹³Institute of Electronic Structure and Laser, Foundation for Research and Technology-Hellas, Voutes, 71110 Heraklion, Greece

¹⁴Janusz Gil Institute of Astronomy, University of Zielona Góra, Prof. Szafrana 2, PL-65-516 Zielona Góra, Poland

Accepted XXX. Received YYY; in original form ZZZ

ABSTRACT

We present uniformly reprocessed and re-calibrated data from the *RoboPol* programme of optopolarimetric monitoring of active galactic nuclei (AGN), covering observations between 2013, when the instrument was commissioned, and 2017. In total, the dataset presented in this paper includes 5068 observations of 222 AGN with Dec $> -25^\circ$. We describe the current version of the RoboPol pipeline that was used to process and calibrate the entire dataset, and we make the data publicly available for use by the astronomical community. Average quantities summarising optopolarimetric behaviour (average degree of polarization, polarization variability index) are also provided for each source we have observed and for the time interval we have followed it.

Key words: galaxies: active – galaxies: jets – galaxies: nuclei – polarization

1 INTRODUCTION

The *RoboPol* Collaboration¹ monitored the optical linear polarization and brightness of a large sample of active galactic nuclei (AGN) from 2013 to 2017, using the *RoboPol* polarimeter (Ramaprakash et al. 2019), which was developed for this project, and which is in-

stalled at the 1.3m telescope of the Skinakas Observatory in Crete, Greece. The main science goal of the *RoboPol* project was to explore a possible link between optical polarization behaviour, particularly the electric vector position angle (EVPA) rotations, and flares in the γ -ray emission of blazars. The main project was run between 2013 May and 2015 November. During this period the monitoring was focused on two well-defined samples: the main sample, consisting of γ -ray loud AGN detected in the *Fermi*–LAT Second Source Catalogue (2FGL, Nolan et al. 2012); and the control sample, consisting of otherwise similar AGN, which however had not

* E-mail: blinov@ia.forth.gr

† Hubble Fellow

¹ <http://robopol.org>

2 D. Blinov *et al.*

been detected by *Fermi*–LAT. The sample selection is discussed in §2 and in greater detail in Pavlidou *et al.* (2014). In addition to the main monitoring programme, we observed additional sources for other projects, also described in §2. Major results based on the data set presented in this paper were published in Pavlidou *et al.* (2014); Blinov *et al.* (2015, 2016a,b, 2018); Angelakis *et al.* (2016); Hovatta *et al.* (2016); Kiehlmann *et al.* (2017); Liidakis *et al.* (2017).

In this paper, we present a complete and uniform reprocessing of all observations in the 5-year AGN monitoring dataset, using the latest version of the *RoboPol* pipeline. The samples of sources that have been included in our monitoring during the programme are summarised in §2. Information on the *RoboPol* polarimeter and the telescope, where it is mounted, is given in §3. The current version of the *RoboPol* pipeline that has been used to process all data presented in this paper is described in §4. Details on the standard stars used for calibration are given in §5. The reader is alerted to caveats that have arisen in the processing of specific sources in §6. The data we release for each source, including individual observations and summary statistics quantifying the optopolarimetric behaviour of each source are described in §7. This data are made publicly available for use by the astronomical community. Our data policy is discussed in §8. The values of EVPA in this work are measured from North to East following the IAU convention (IAU Commission 40 1974). All monitoring data made available in this paper are not corrected for positive bias of the polarization fraction (Serkowski 1958).

With this paper we publish 5068 polarimetric measurements of 222 AGN located at Dec $>-25^\circ$ obtained during the 2013 – 2017 observing seasons.

2 OBSERVING SAMPLES

We provide data for sources belonging to several observing samples as indicated by the ‘sample’ flag in the data Table A. Here, we briefly describe these samples, and we refer the reader to the corresponding results-and-analysis papers for more details.

During, and immediately after, the *RoboPol* polarimeter commissioning, we performed a month-long single-epoch survey of two unbiased samples of 89 γ -ray-loud (Sample Identifier SID=1, see Table A) and 15 γ -ray-quiet (SID=2) sources. The details of the sample selection are described in Pavlidou *et al.* (2014).

During the main monitoring programme, we regularly observed sources belonging to two samples: the ‘main’ γ -ray-loud sample (SID=3), consisting of 62 sources selected by placing a photon-flux cut on sources from the Second Fermi LAT Catalogue (2FGL, Nolan *et al.* 2012) and an additional optical magnitude cut, as well as constraints on source visibility and separation from other field sources; and the ‘control’ γ -ray-quiet sample (SID=4), of 15 sources selected based on their radio variability properties and absence from 2FGL. Control sample sources were selected from non-2FGL sources from CGRaBS (Candidate Gamma-Ray Blazar Survey, Healey *et al.* 2008) placing a 15 GHz flux density cut, and identical optical magnitude, visibility, and field-quality cuts as for the γ -ray-loud sample. Among all sources satisfying these criteria, we selected the ones that were most variable in radio, as quantified by their 15 GHz modulation index (Richards *et al.* 2011). Slight changes to the initial ‘control’ sample were made in Blinov *et al.* (2016a,b, 2018) because two of the γ -ray-quiet sources appeared in the Third Fermi LAT Catalogue (3FGL Acerò *et al.* 2015). For this reason we added two more sources satisfying our selection criteria that were not present in any of the Fermi LAT catalogues.

In addition to the ‘main’ and ‘control’ samples, during 2013 – 2014 we monitored a sample of 24 individually-selected sources of high interest. Moreover, 44 other AGN were observed for different projects along the project execution. These sources that have *not* been selected with uniform criteria are assigned SID=5. In 2014 we also conducted a distinct polarization monitoring programme focused on intermediate- and high-synchrotron peaked BL Lac objects. This programme included 29 TeV-detected sources and 19 non-TeV sources, collectively described in Table A with SID=6. Details of the selection criteria for these samples are described in Hovatta *et al.* (2016).

3 TELESCOPE AND POLARIMETER

Optical polarimetric observations were performed using the 1.3-m telescope at the Skinakas Observatory² in Crete (1750 m.a.s.l., $35^\circ 12' 43''$ N, $24^\circ 53' 57''$ E). The telescope is equipped with the *RoboPol* imaging polarimeter (Ramaprakash *et al.* 2019), which was designed specifically for this monitoring programme. *RoboPol* is comprised of two adjacent half-wave retarders with fast-axes rotated by 67.5° with respect to each other. They are followed by two Wollaston prisms with orthogonal fast-axes. This configuration splits every incident ray into two pairs of spots on the CCD that carry information about Q/I and U/I normalised Stokes parameters in the instrument reference frame (see Eq. 1 in King *et al.* 2014). In the case when a photometric standard with known magnitude is in the field, the total intensity or Stokes I parameter can be obtained together with Q/I and U/I with a single exposure. Unfortunately, only a small fraction of sources in our samples has accurately measured robust photometric standards in their fields. Therefore, here we present only normalised Stokes parameters without the total flux data. Since the instrument has no moving parts other than the filter wheel, it is relieved of random and systematic errors due to sky changes between measurements, imperfect alignment and non-uniformity of rotating optical elements. In order to increase the SNR (signal-to-noise ratio) for the central target measurements, a mask of a special shape was introduced in the centre of the focal plane. An example of an image obtained with *RoboPol* is shown in Fig. 1.

The polarimeter is equipped with a 2048×2048 pixels ANDOR DW436 CCD with a $13.5\text{ }\mu\text{m}$ pixel size. It provides a scale of $0.435\text{ arcsec pixel}^{-1}$ and a field of view (FoV) of $13 \times 13\text{ arcmin}^2$. All observations described in this paper were made with a Johnson-Cousins *R*-band filter.

4 ROBOPOL PIPELINE

The *RoboPol* pipeline was planned and implemented to be capable of working with no user intervention. It is able to derive the magnitude and linear polarization of every unobscured source in the field (i.e. every source that is not blocked by the focal plane mask and its holders). The pipeline is written in Python, with some procedures written in Cython to improve performance. A detailed description of the pipeline is presented by King *et al.* (2014). Upgrades in the pipeline designed to optimize performance for field sources are discussed in Panopoulou *et al.* (2015). In the following sections we describe only recent upgrades in the pipeline that have not been described elsewhere.

² <http://skinakas.physics.uoc.gr>

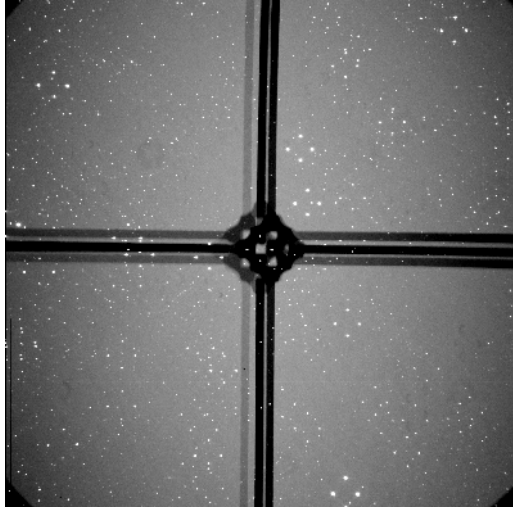


Figure 1. An example of a *RoboPol* image. Each point in the sky is mapped to four spots on the CCD. A focal plane mask, held in place by four support legs, reduces the sky background level for the central target.

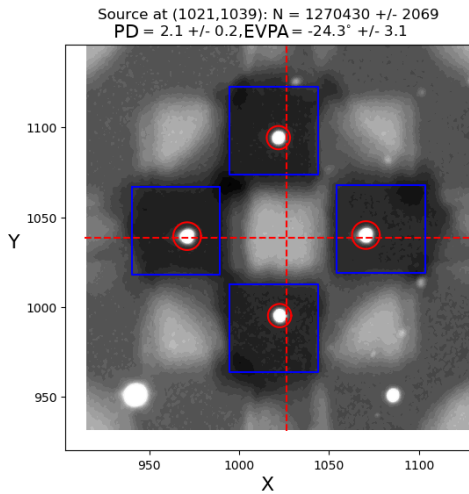


Figure 2. Masked central area of the RoboPol image with the central science target. The red circles are the photometry apertures. The blue squares are the automatically identified background estimation areas for the central science target.

4.1 Upgrades of the pipeline

4.1.1 Mask location and background estimates

The main science targets are positioned within the central, masked area of the *RoboPol* image shown in Fig. 2. The sky background for each source spot is estimated within the corresponding masked areas (the blue squares in Fig. 2). The four squares pattern is automatically identified by the pipeline. First versions of the pipeline considered this pattern as a whole. However, it was found that the relative positions of the shadows are variable within ~ 10 pix. Therefore, the latest version of the pipeline locates each square separately. This provides more accurate histograms of the background counts, preventing biasing of the background estimate towards brighter values.

The default background estimation method used in the pipeline has been changed to a procedure similar to the one used in SExtractor

(Bertin & Arnouts 1996). The procedure consists of the following steps. (1) The histogram of pixel values within the masked square is iteratively sigma-clipped, with 2.7σ as the limit. (2) If the sigma-clipped σ changed more than 20 per cent from its initial value, the histogram is considered to be skewed, and the background value is estimated using $\text{Mode} = 2.5 \times \text{Median} - 1.5 \times \text{Mean}$. Otherwise, the mean of the clipped histogram is taken as the value for the background.

The background histograms and calculated background values for all measurements in this paper have been visually inspected. In the cases where the default method provided unsatisfactory results, the images were reprocessed using one of the other algorithms implemented in the pipeline. These include the following: (a) Mean value of the background pixels; (b) Mode of the background pixels; (c) The original background estimation procedure described in King et al. (2014), which searches for the centroid in the sigma-clipped and smoothed histogram of background pixels values.

4.1.2 Aperture photometry

The full width at half maximum (FWHM) of the vertical pair of spots is different from that of the horizontal pair (see Fig. 2), due to the instrument design. The optimal size of the photometry aperture, which minimizes the uncertainties, depends on the FWHM. Therefore, the current version of the pipeline measures and treats two pairs of spots independently.

For AGN with prominent host galaxies, measured polarization values are reduced by unpolarized emission of the host inside the aperture. This depolarization effect varies with seeing: fractional polarization is lower for shots with larger FWHM (Sosa et al. 2017). In order to minimize this effect for sources with bright hosts we used fixed apertures 3 arcsec to 6 arcsec in diameter depending on the source. The corresponding value for each source is given in the ‘aperture’ column of Table A1. All other unresolved objects or sources with negligible host galaxy contribution were measured with aperture dependent on FWHM that optimised SNR. We processed each source with 8 different apertures with sizes in the range $1 - 4.5 \times \text{FWHM}$. Then we visually verified that the fractional polarization and EVPA stabilised within this range of apertures. Finally, we selected the aperture size that provided the highest SNR in fractional polarization in the stability range. This value was 5.1 arcsec on median.

4.1.3 Centroids of the main target spots

The pipeline uses SExtractor (Bertin & Arnouts 1996) for identification of sources in the image. It provides a windowed centroid position for each source in the frame. In a small fraction of images with a strong gradient of the sky background at the edges of the masked regions, the centroid calculation procedure fails. This causes inaccurate polarization measurements of the central target. In order to avoid this problem, we have added a second procedure for centroid computation, based on the PyGuide³ library. After the identification of the central target spots in the SExtractor output catalogue, the pipeline finds parameters $\Delta_x, \delta_x, \phi_x, \Delta_y, \delta_y$ and ϕ_y of the spatial distortions model, whose meaning is demonstrated in Fig. 3 (see also §2.2.1 in King et al. (2014)). If any of these parameters deviates from the model prediction more than the maximum residual in the model fit (see § 4.2 and Fig. B2, B3), then the spots

³ <http://staff.washington.edu/rowen/PyGuide/Manual.html>

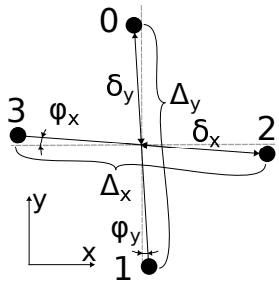


Figure 3. The pattern of 4 spots at each position (x, y) on the CCD and 6 parameters describing it. $\Delta_x(x, y)$ is the distance between the horizontal spots, $\delta_x(x, y)$ is the distance from the right-spot to the central point, and $\phi_x(x, y)$ is the angle between the CCD x-axis and the line connecting horizontal points. $\Delta_y(x, y)$, $\delta_y(x, y)$ and $\phi_y(x, y)$ denote similar quantities for the vertical pair of spots.

centroids calculation is considered to have failed. In this case the second PyGuide based centroid computation algorithm is used. The combination of both algorithms has proven sufficient in practice. We have not identified any image in our observations where both methods fail.

4.1.4 Additional astrometry procedure

The *RoboPol* pipeline uses the Astrometry.net (Lang et al. 2010) library to perform astrometry. Accurate coordinates of the field sources are needed for the pointing procedure during observations and for the differential photometry during the data processing. In the case of a bright sky or very sparse stellar field (e.g. in some of the fields studied in Skalidis et al. 2018, or AGN at high galactic latitudes) Astrometry.net is unable to find a solution for the World Coordinate System. For this reason we have added a second astrometry routine which is based on the Alipy⁴ library. This routine starts only if Astrometry.net fails. It finds a geometrical transformation between the current frame and a preliminary stored source catalogue, which has a World Coordinate System (WCS) solution. Then the calculated transformation in the CCD frame is converted to WCS transformation and, thereby, the new WCS of the current frame is defined. This routine requires either a previous *RoboPol* image of the same field solved by Astrometry.net or the Digitized Sky Survey fits image with a WCS solution in the header.

4.1.5 Polarization measurements statistics

Values of PD and its uncertainty were calculated following Eq. 5 in King et al. (2014) under the assumption of Gaussianity of the Stokes parameters. Any linear polarization measurement is subject to bias towards higher polarization degree (PD) values (Serkowski 1958). The PD follows the Rice (1945) distribution, which deviates significantly from the normal distribution at low SNR. Since there is a variety of methods suggested for correction of this bias (e.g. Simmons & Stewart 1985; Vaillancourt 2006; Plaszczynski et al. 2014) we did not include any bias correction of the fractional polarization into the pipeline. **The monitoring data discussed in this paper is uncorrected for bias.**

EVPA measurements are also non-Gaussian and defined by the

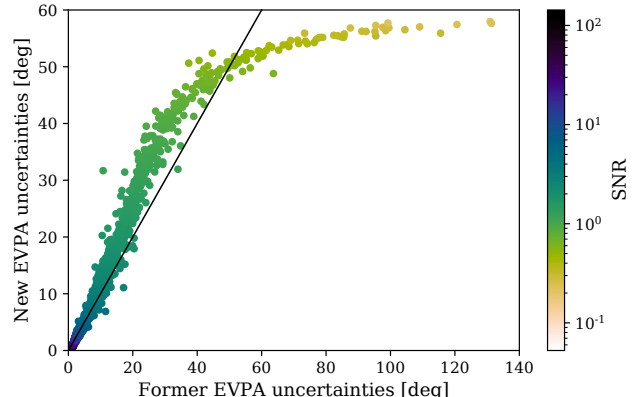


Figure 4. New EVPA uncertainty estimates calculated according to § 4.1.5 plotted against the former estimates calculated according to King et al. (2014). The solid line is $y=x$. The colour coding shows the signal-to-noise-ratio of the polarization fraction.

following probability density (Naghizadeh-Khouei & Clarke 1993):

$$G(\text{EVPA}, \text{EVPA}_0, \text{PD}_0) =$$

$$= \frac{1}{\sqrt{\pi}} \left\{ \frac{1}{\sqrt{\pi}} + \eta_0 \exp\left(\eta_0^2\right) [1 + \text{erf}(\eta_0)] \right\} \exp\left(-\frac{\text{PD}_0^2}{2\sigma_{\text{PD}}^2}\right), \quad (1)$$

where $\eta_0 = \text{PD}_0 \cos 2(\text{EVPA} - \text{EVPA}_0) / (\sigma_{\text{PD}} \sqrt{2})$, erf is the Gaussian error function, PD_0 and EVPA_0 are the true values of PD and EVPA and σ_{PD} is the uncertainty of PD.

In the latest version of the pipeline we determine the EVPA uncertainty σ_{EVPA} numerically solving the following integral:

$$\int_{-1\sigma_{\text{EVPA}}}^{1\sigma_{\text{EVPA}}} G(\text{EVPA}, \text{PD}_0) d\text{EVPA} = 0.6827. \quad (2)$$

The true PD value in this procedure is estimated using the Modified ASymptotic (MAS) estimator proposed by Plaszczynski et al. (2014) as follows:

$$\text{PD}_0 = \text{PD} - \sigma_{\text{PD}}^2 \frac{1 - \exp(-\text{PD}^2/\sigma_{\text{PD}}^2)}{2\text{PD}} \quad (3)$$

For high SNR values $\text{PD}/\sigma_{\text{PD}} \geq 10$ the uncertainty of EVPA is approximated as $\sigma_{\text{EVPA}} = 0.5\sigma_{\text{PD}}/\text{PD}_0$.

Figure 4 shows the new EVPA uncertainty estimates plotted against the former estimates calculated with the previous pipeline as described in King et al. (2014). The uncertainties tend to have been underestimated in moderately low SNR ($1 \lesssim \text{SNR} \lesssim 10$) and to have been overestimated in very low SNR < 1 .

4.2 Instrument model

Instrumental polarization, vignetting and spatial distortions of the four-spots-pattern are corrected by the instrument model. The instrument model consists of two independent parts. The first part approximates the dependencies of the six parameters in Fig. 3 on the (x, y) -position on the CCD. The second part is a spatial function that describes multipliers for photon counts in each of the four spots as a function of (x, y) . These multipliers compensate for the global variations of the instrumental polarization in the field and vignetting. The instrument model coefficients are obtained by fitting the model to measurements from a raster scan of a zero-polarized

⁴ <https://obswww.unige.ch/~tewes/alipy/>

star in the field. The complete description of the *RoboPol* instrument model was presented by King et al. (2014).

The instrument response can vary with time, telescope position, flexure, temperature etc. For this reason, we performed a raster scan of a zero-polarized star several times per season and after every removal of the *RoboPol* polarimeter from the telescope. During the 2013 – 2017 period we obtained 11 model scans using 7 different zero-polarized standards in different positions of the telescope. Comparing results of the model fit to these data, we do not find any significant systematic difference between these models.

Combining multiple model raster scans of zero-polarized stars that were observed at different epochs, we are able to reduce the random errors of the model fits. Therefore, for the data discussed in this paper we used the combined model. It was created using 1624 measurements of unpolarized stars in all 11 raster scans obtained in 2013 – 2017 and shown in Fig. B1 of Appendix B. Figures B2 – B7 of the same appendix show the fits of model parameters and their residuals. This model gives the best approximation of the instrumental polarization and is less noise-dominated than any single raster scan.

5 CALIBRATION USING STANDARD STARS

The instrument model accounts for the variation of the polarization response of the instrument globally across the FoV, while all AGN were measured in the narrow central masked area. Since the model can deviate locally from the real instrumental polarization value we have also been monitoring polarimetric standard stars in the mask. The list of stars observed during the project execution period and their catalogued polarization values together with corresponding references are given in Table 1. We note that some stars monitored in the project turned out to be variable, despite the fact that they are considered as standards in other polarimetric programmes and literature. For example, we certainly observe variability in HD 204827, HD 183143 and VI Cyg 12, which is in agreement with Hsu & Breger (1982); Dolan & Tapia (1986). Moreover, some standards appear to be stable but their polarization significantly deviates from that reported in the literature (e.g. CMaR1 24 and BD+57.2615). Furthermore, the situation is complicated by multiple inconsistent polarimetric parameters reported in different works for some standards. In general, the situation with optical polarimetric standards can be characterised as disheartening. For this reason in 2018 we started an effort intended to establish a well defined sample of stable polarimetric standards. Its results will be reported elsewhere.

Figure 5 shows the distribution of relative Stokes parameters of zero-polarized standards measured along the whole observing period. Measurements of WD2149+021 systematically deviate from the centroid of all other measurements. Therefore, this star was excluded from the analysis. The weighted mean centroid for all other measurements in Fig. 5 is located at $Q/I = -0.0015$, $U/I = -0.0004$. This value is the difference between the model-predicted and the real instrumental polarization at the central mask region. We used this quantity as an additional instrument polarization correction for all AGN measurements. The standard deviations of the Stokes parameters in Fig. 5 are 0.0014 and 0.0011. These values were considered as uncertainties and propagated to the AGN measurements uncertainties. It is worth noting that in this work we use a different approach from the one reported in Ramaprakash et al. (2019), where polarization standards were processed without the instrument model correction. There, it was found that the instrumental polarization varies between observing seasons with an amplitude

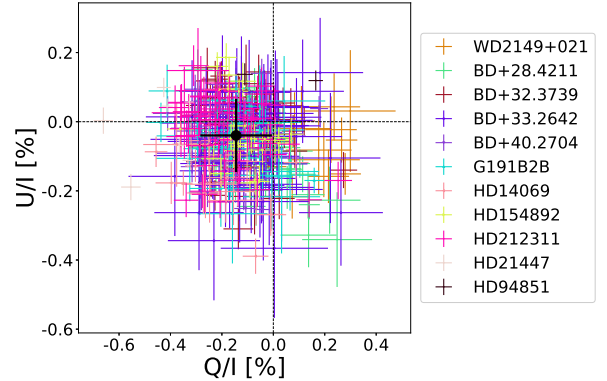


Figure 5. Relative Stokes parameters of zero-polarization standards observed in 2013 – 2017. The weighted mean is shown by the black point.

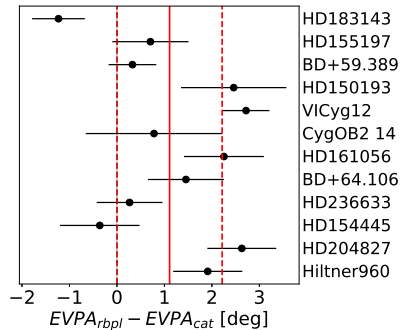


Figure 6. Differences between weighted average of observed EVPA and corresponding catalogue values for 12 most reliable highly-polarized standards. Weighted mean value for all 12 stars is shown by the solid red line, while their weighted standard deviation is shown by the red dashed lines.

$\sim 0.1 - 0.2$ per cent. This variation can be partly explained by the fact that the mask shadow location on the CCD changes slightly with time. Unlike Ramaprakash et al. (2019), in this work we use the instrument model correction of polarization parameters, which accounts for changing position of a target on the CCD. Presumably for this reason we do not find any significant variability of the instrumental polarization among observing seasons. Thus, here we use the constant instrumental polarization correction value for all measurements. Even if a residual systematic error is present in such an instrumental polarization correction, its value is negligible compared to typical photon noise of our AGN measurements.

In order to find the rotation of the instrumental Q/I - U/I plane with respect to the standard reference frame we used 331 observations of 12 high-polarization stars that are considered to be the most stable standards. The difference between catalogued and averaged *RoboPol* values of EVPA for these stars are shown in Fig. 6. The weighted average for 12 stars is $EVPA_{rbpl} - EVPA_{cat} = 1.1 \pm 1.1^\circ$. Relative Stokes parameters Q/I and U/I of AGN were corrected for this EVPA zero point offset and the uncertainties were propagated.

6 NOTES ON INDIVIDUAL SOURCES

In this section we list caveats that arose during the processing of individual sources in the sample.

J0035+5950: A source of comparable brightness is located 1.58 arcsec from the blazar. It was initially considered as the

Table 1. Polarization parameters of standard stars monitored by *RoboPol*, as reported in the literature.

Source	Band	PD (%)	EVPA (°)	Reference
polarized				
BD+57.2615	R	2.02 ± 0.05	41.0 ± 1.0	Whittet et al. (1992)
BD+59.389	R	6.430 ± 0.022	98.14 ± 0.10	Schmidt et al. (1992)
BD+64.106	R	5.150 ± 0.098	96.74 ± 0.54	Schmidt et al. (1992)
CMaR1 24	R	3.18 ± 0.09	86.0 ± 1.0	Whittet et al. (1992)
CygOB2 14	R	3.13 ± 0.05	86.0 ± 1.0	Whittet et al. (1992)
HD147283	R	1.59 ± 0.03	174.0 ± 1.0	Whittet et al. (1992)
	R	1.81	176.0	Carrasco et al. (1973)
HD147343	R	0.43 ± 0.05	151.0 ± 3.0	Whittet et al. (1992)
HD150193	R	5.19 ± 0.05	56.0 ± 1.0	Whittet et al. (1992)
HD154445	R	3.683 ± 0.072	88.91 ± 0.56	Schmidt et al. (1992)
	R	3.63 ± 0.01	90.0 ± 0.1	Hsu & Breger (1982)
HD155197	R	4.274 ± 0.027	102.88 ± 0.18	Schmidt et al. (1992)
HD161056	R	4.012 ± 0.032	67.33 ± 0.23	Schmidt et al. (1992)
HD183143 ^b	R	5.90 ± 0.05	179.2 ± 0.2	Hsu & Breger (1982)
	R	5.7 ± 0.04	178.0 ± 1.0	Bailey & Hough (1982)
HD204827 ^b	R	4.893 ± 0.029	59.10 ± 0.17	Schmidt et al. (1992)
	R	4.86 ± 0.05	60.0 ± 1.0	Bailey & Hough (1982)
	R	4.99 ± 0.05	59.9 ± 0.1	Hsu & Breger (1982)
HD215806	R	1.83 ± 0.04	66.0 ± 1.0	Whittet et al. (1992)
HD236633	R	5.376 ± 0.028	93.04 ± 0.15	Schmidt et al. (1992)
Hiltner960 ^a	R	5.210 ± 0.029	54.54 ± 0.16	Schmidt et al. (1992)
VICyg12 ^b	R	7.97 ± 0.05	117.0 ± 1.0	Whittet et al. (1992)
	R	7.893 ± 0.037	116.23 ± 0.14	Schmidt et al. (1992)
	R	7.18 ± 0.04	117.0 ± 1.0	Hsu & Breger (1982)
unpolarized				
BD+28.4211	V	0.054 ± 0.027	54.22	Schmidt et al. (1992)
BD+32.3739	V	0.025 ± 0.017	35.79	Schmidt et al. (1992)
BD+33.2642	R	0.20 ± 0.15	78 ± 20	Skalidis et al. (2018)
BD+40.2704	?	0.07 ± 0.02	57 ± 9	Berdyugin & Teerikorpi (2002)
G191B2B	V	0.061 ± 0.038	147.65	Schmidt et al. (1992)
HD14069	V	0.022 ± 0.019	156.57	Schmidt et al. (1992)
HD154892	B	0.05 ± 0.03	-	Turnshek et al. (1990)
HD212311	V	0.034 ± 0.021	50.99	Schmidt et al. (1992)
HD21447	V	0.051 ± 0.020	171.49	Schmidt et al. (1992)
HD94851	B	0.057 ± 0.018	-	Turnshek et al. (1990)
WD2149+021	R	0.050 ± 0.006	-63 ± 3	Cikota et al. (2017)

^a - possibly variable You et al. (2017); ^b - variable in *RoboPol* data or/and in Hsu & Breger (1982); Dolan & Tapia (1986);

lensed image of the blazar, however it was not detected in radio (Aleksić et al. 2015). Due to the small separation between the two sources, it could not be resolved in all seeing conditions in *RoboPol* images. For this reason we performed the aperture photometry with a fixed 6 arcsec aperture surrounding both sources. Therefore, the polarization fraction values are most likely significantly underestimated, while the EVPA should be reliable.

J0324+3410: For this source we used a fixed 4 arcsec aperture. However, this Narrow-Line Seyfert 1 (NLSy1) has asymmetric spiral arms resolved in the host galaxy (Zhou et al. 2007). The spiral arms can potentially give non-zero polarization of the stellar light. A dedicated study is needed to clarify whether the starlight of the host has significant polarization.

J0728+5701: A foreground star is located nearby. To avoid depolarization due to contamination by the star light we used a fixed 4 arcsec aperture.

J0849+5108: This NLSy1 has a prominent spiral host galaxy (Hamilton et al. 2020). It appears to be asymmetric in images and can potentially contribute to the polarization. We measured the nucleus with a fixed 4 arcsec aperture.

J1148+5924: NGC 3894 has a very bright host. The galaxy fills the masked areas entirely. For this reason there is a possibility of deviation of the PD from its real values due to inaccurate estimate

of the sky background. We measured this source with a fixed 6 arcsec aperture.

J1442+1200: 1ES 1440+122 has a prominent host galaxy. There is also a nearby source located 2.5 arcsec from the core according to Gaia data (Gaia Collaboration et al. 2018). It could potentially affect the polarization. We measured the nucleus with a fixed 4.5 arcsec aperture.

J1505+0326: This NLSy1 has a prominent elliptical host galaxy, however there is an asymmetric structure 3 arcsec from the core that is probably produced by an interaction with another galaxy (D’Ammando et al. 2018). Since we measured the source with a fixed 4 arcsec aperture the emission of this component can potentially contribute to the polarization.

J1653+3945: Mkn501 has a very bright host. The galaxy fills the masked areas entirely. For this reason there is a possibility of deviation of the PD from its real values due to inaccurate estimate of the sky background. We measured this source with a fixed 6 arcsec aperture.

J1728+0427: PKS 1725+044 has a prominent host galaxy. There is also a nearby source located 1.6 arcsec from the core according to Gaia data. It could potentially affect the polarization. We measured the nucleus with a fixed 4 arcsec aperture.

J1733–1304: PKS 1730–130 has a nearby source located 1.8 arc-

sec from the core according to Gaia data. It could potentially affect the polarization. We measured the nucleus with a fixed 5 arcsec aperture.

J1743+1935: This AGN has a prominent host galaxy. There is also a nearby source located 3.4 arcsec from the core according to Gaia data. It could potentially affect the polarization. We measured the nucleus with a fixed 5 arcsec aperture.

J1943+2118: A few measurements for this TeV source have been presented in (Hovatta et al. 2016). However, reanalysing data for this paper, we discovered that the source was previously misassociated. The measured polarization corresponds to a ~ 17 mag star, while the TeV AGN is associated with 2MASS source J1943562+2118233 (Landi et al. 2009) that is located 5.3 arcsec North-West from this star. Since the AGN is very faint $R \approx 22.4$ mag, it cannot be measured in our images. For this reason J1943+2118 is not present in the data table.

J2031+1219: There is a nearby source located 2.9 arcsec from the core according to Gaia data. It could potentially affect the polarization. We measured the nucleus with a fixed 3 arcsec aperture.

J2033+2146: This AGN has a prominent host galaxy. There is also a nearby foreground star located 2.3 arcsec from the core according to Gaia data. It could potentially affect the polarization. We measured the nucleus with a fixed 4 arcsec aperture.

7 MONITORING DATA AND POLARIZATION PARAMETERS

The data products that are made publicly available in this work are the polarimetric monitoring data of the sample sources and their average polarization parameters. Machine-readable form of the data tables can be accessed via Harvard dataverse⁵ and Vizier. Abridged versions of the average polarization parameters table and monitoring data table are also presented in the Appendix A.

In Table A1 of Appendix A we list general information about AGN in the sample including their equatorial coordinates, redshift with corresponding reference and their sample ID. We also give the total number of observations of each source, and the number of seasons during which it has been observed, and the median time sampling interval. Additionally, we provide the following statistics to quantify the average and variability of the fractional polarization and the EVPA. We estimate the intrinsic mean polarization fraction p_0 and the intrinsic modulation index m_p by modelling the distribution of the measured polarization fraction as a Beta distribution following Blinov et al. (2016a). We infer the distribution parameters with Bayesian modelling using PyStar⁶. To quantify the EVPA variability we take the difference of the 75 per cent and 25 per cent quantiles of the measured EVPA distribution. We subtract this value from 180° if the difference exceeds 90° . The result is divided by 90° . This variability index, v_χ , is normalised to the interval $[0, 1]$, where 0 corresponds to a perfectly stable EVPA and 1 corresponds to a variable EVPA with a perfectly uniform distribution, i.e. no preferred orientation. For sources with $v_\chi < 0.5$ we show the wrap-corrected median EVPA as a measure of the preferred orientation.

The entire AGN monitoring data are given in electronic format, while the first rows of this table are given in Table A2. There for each

observation we provide Julian Date (JD), relative Stokes parameters and their uncertainties before the instrument polarization correction, relative Stokes parameters after the instrument polarization and EVPA zero-point correction as well as corresponding values of PD and EVPA.

8 DATA POLICY

These data are being made available to the public as a service to the astronomical community. If you use RoboPol data in your research, we request that you cite the present publication, allowing us to keep track of the impact of our work, and that you include the following acknowledgement: 'This research has made use of data from the RoboPol programme, a collaboration between Caltech, the University of Crete, IA-FORTH, IUCAA, the MPIfR, and the Nicolaus Copernicus University, which was conducted at Skinakas Observatory in Crete, Greece.'

ACKNOWLEDGEMENTS

We thank A. Steiakaki and E. Paleologou for their invaluable contribution and technical support. The RoboPol project is a collaboration between Caltech in the USA, MPIfR in Germany, Toruń Centre for Astronomy in Poland, the University of Crete/FORTH in Greece, and IUCAA in India. The U. of Crete group acknowledges support by the "RoboPol" project, which was implemented under the "Aristeia" Action of the "Operational Programme Education and Lifelong Learning" and was co-funded by the European Social Fund (ESF) and Greek National Resources, and by the European Comission Seventh Framework Programme (FP7) through grants PCIG10-GA-2011-304001 "JetPop" and PIRSES-GA-2012-31578 "EuroCal". This research was supported in part by NASA grant NNX11A043G and NSF grant AST-1109911, and by the Polish National Science Centre, grant numbers 2011/01/B/ST9/04618 and 2017/25/B/ST9/02805. C.C., D.B., N.M., R.S. and K.T. acknowledge support from the European Research Council (ERC) under the European Union Horizon 2020 research and innovation programme under the grant agreement No 771282. K.T. and G.V.P. acknowledge support by the European Commission Seventh Framework Programme (FP7) through the Marie Curie Career Integration Grant PCIG-GA-2011-293531 "SFOnset" as well as NASA Hubble Fellowship grant # HST-HF2-51444.001-A awarded by the Space Telescope Science Institute, which is operated by the Association of Universities for Research in Astronomy, Incorporated, under NASA contract NAS5-26555. T.H. was supported by the Academy of Finland projects 317383, 320085, and 322535

DATA AVAILABILITY

The data underlying this article are available in Harvard Dataverse, at <https://dx.doi.org/10.7910/DVN/IMQKSE>.

REFERENCES

- Acero F., et al., 2015, *ApJS*, 218, 23
- Aleksić J., et al., 2015, *MNRAS*, 446, 217
- Angelakis E., et al., 2016, *MNRAS*, 463, 3365
- Bailey J., Hough J. H., 1982, *PASP*, 94, 618
- Berdugan A., Teerikorpi P., 2002, *A&A*, 384, 1050

⁵ <https://doi.org/10.7910/DVN/IMQKSE>

- Bernardi M., Alonso M. V., da Costa L. N., Willmer C. N. A., Wegner G., Pellegrini P. S., Rité C., Maia M. A. G., 2002, [AJ](#), **123**, 2990
- Bertin E., Arnouts S., 1996, [A&AS](#), **117**, 393
- Blinov D., et al., 2015, [MNRAS](#), **453**, 1669
- Blinov D., et al., 2016a, [MNRAS](#), **457**, 2252
- Blinov D., et al., 2016b, [MNRAS](#), **462**, 1775
- Blinov D., et al., 2018, [MNRAS](#), **474**, 1296
- Carrasco L., Strom S. E., Strom K. M., 1973, [ApJ](#), **182**, 95
- Cikota A., Patat F., Cikota S., Faran T., 2017, [MNRAS](#), **464**, 4146
- Cohen J. G., Lawrence C. R., Blandford R. D., 2003, [ApJ](#), **583**, 67
- D'Ammando F., Acosta-Pulido J. A., Capetti A., Baldi R. D., Orienti M., Raiteri C. M., Ramos Almeida C., 2018, [MNRAS](#), **478**, L66
- Dolan J. F., Tapia S., 1986, [PASP](#), **98**, 792
- Falomo R., Kotilainen J. K., 1999, [A&A](#), **352**, 85
- Furniss A., Fumagalli M., Danforth C., Williams D. A., Prochaska J. X., 2013, [ApJ](#), **766**, 35
- Gaia Collaboration et al., 2018, [A&A](#), **616**, A1
- Hamilton T., Foschini L., Berton M., 2020, in American Astronomical Society Meeting Abstracts. American Astronomical Society Meeting Abstracts. p. 304.10
- Healey S. E., et al., 2008, [ApJS](#), **175**, 97
- Hewitt A., Burbidge G., 1987, [ApJS](#), **63**, 1
- Hovatta T., et al., 2016, [A&A](#), **596**, A78
- Hsu J.-C., Breger M., 1982, [ApJ](#), **262**, 732
- Hughes P. A., Aller H. D., Aller M. F., 1992, [ApJ](#), **396**, 469
- IAU Commission 40 1974, in G. Contopoulos and A. Jappel ed., Transactions of the IAU. Vol. XVIB. Reidel, Dordrecht, p. p.166
- Jones D. H., et al., 2009, [MNRAS](#), **399**, 683
- Kiehlmann S., Blinov D., Pearson T. J., Liodakis I., 2017, [MNRAS](#), **472**, 3589
- King O. G., et al., 2014, [MNRAS](#), **442**, 1706
- Landi R., et al., 2009, [A&A](#), **493**, 893
- Lang D., Hogg D. W., Mierle K., Blanton M., Roweis S., 2010, [AJ](#), **139**, 1782
- Laurent-Muehleisen S. A., Kollgaard R. I., Ciardullo R., Feigelson E. D., Brinkmann W., Siebert J., 1998, [ApJS](#), **118**, 127
- Liodakis I., Blinov D., Papadakis I., Pavlidou V., 2017, [MNRAS](#), **465**, 4783
- Meisner A. M., Romani R. W., 2010, [ApJ](#), **712**, 14
- Murphy D. W., Browne I. W. A., Perley R. A., 1993, [MNRAS](#), **264**, 298
- Naghizadeh-Khouei J., Clarke D., 1993, [A&A](#), **274**, 968
- Neronov A., Semikoz D., Taylor A. M., Vovk I., 2015, [A&A](#), **575**, A21
- Nolan P. L., et al., 2012, [ApJS](#), **199**, 31
- Osmor P. S., Porter A. C., Green R. F., 1994, [ApJ](#), **436**, 678
- Panopoulou G., et al., 2015, [MNRAS](#), **452**, 715
- Pavlidou V., et al., 2014, [MNRAS](#), **442**, 1693
- Pita S., et al., 2014, [A&A](#), **565**, A12
- Plaszczynski S., Montier L., Levrier F., Tristram M., 2014, [MNRAS](#), **439**, 4048
- Ramaprakash A. N., et al., 2019, [MNRAS](#), **485**, 2355
- Rice S. O., 1945, Bell Systems Tech. J., Volume 24, p. 46-156, [24](#), 46
- Richards J. L., et al., 2011, [ApJS](#), **194**, 29
- Schachter J. F., et al., 1993, [ApJ](#), **412**, 541
- Schmidt G. D., Elston R., Lupie O. L., 1992, [AJ](#), **104**, 1563
- Serkowski K., 1958, Acta Astron., [8](#), 135
- Shaw M. S., et al., 2013, [ApJ](#), **764**, 135
- Simmons J. F. L., Stewart B. G., 1985, [A&A](#), **142**, 100
- Skalidis R., Panopoulou G. V., Tassis K., Pavlidou V., Blinov D., Komis I., Liodakis I., 2018, [A&A](#), **616**, A52
- Sosa M. S., von Essen C., Andruchow I., Cellone S. A., 2017, [A&A](#), **607**, A49
- Sowards-Emmerd D., Romani R. W., Michelson P. F., Healey S. E., Nolan P. L., 2005, [ApJ](#), **626**, 95
- Stadnik M., Romani R. W., 2014, [ApJ](#), **784**, 151
- Stocke J. T., Morris S. L., Gioia I. M., Maccacaro T., Schild R., Wolter A., Fleming T. A., Henry J. P., 1991, [ApJS](#), **76**, 813
- Turnshek D. A., Bohlin R. C., Williamson II R. L., Lupie O. L., Koornneef J., Morgan D. H., 1990, [AJ](#), **99**, 1243
- Vaillancourt J. E., 2006, [PASP](#), **118**, 1340
- Whittet D. C. B., Martin P. G., Hough J. H., Rouse M. F., Bailey J. A., Axon D. J., 1992, [ApJ](#), **386**, 562
- You C., et al., 2017, [ApJ](#), **834**, 182
- Zhou H., et al., 2007, [ApJ](#), **658**, L13

APPENDIX A: SAMPLE SOURCES INFORMATION AND MONITORING DATA

Table A1 lists the monitored sources, additional source information, and polarization statistics as described in § 7.

Table A1. Information on the sample sources. (1) - J2000 name; (2) - Alternative source identifier; (3) - Right ascension; (4) - Declination; (5) - Redshift; (6) - Redshift reference; (7) - Sample identifier; (8) - Aperture; (9) - Number of measurements; (10) - Number of seasons; (11) - Median time sampling interval; (12) - Mean intrinsic polarisation fraction; (13) - Intrinsic modulation index of the polarization fraction; (14) - Variability index of the EVPA; (15) - Preferred EVPA orientation of less variable sources. The entire table is available online.

Name	Alt. name	RA (J2000) h:m:s	DEC (J2000) °:':"	z^a	z ref.	SID ^b	Aperture ^c arcsec	N meas.	N seas.	sampling d	p_0 %	m_p	ν_χ	χ_0 deg
(1)	(2)	(3)	(4)	(5)	(6)	(7)	(8)	(9)	(10)	(11)	(12)	(13)	(14)	(15)
RBPLJ0006–0623	PKS 0003–066	00:06:13.9	−06:23:35.3	0.34668	Jones et al. (2009)	5	v	15	2	8	21.20	0.45	0.13	−14.0
RBPLJ0017+8135	S5 0014+81	00:17:08.5	+81:35:08.1	3.366	Osmer et al. (1994)	2,4	v	30	3	7	0.80	0.62	0.65	−
RBPLJ0035+5950	1ES 0033+595	00:35:52.7	+59:50:04.2	0.086	Falomo & Kotilainen (1999)	5	6	5	1	8	−	−	−	−
RBPLJ0045+2127	−	00:45:19.3	+21:27:40.0	−	−	3	v	64	4	3	4.83	0.59	0.84	−
RBPLJ0102+5824	TXS 0059+581	01:02:45.8	+58:24:11.1	0.644	Sowards-Emmerd et al. (2005)	5	v	18	3	9	13.45	0.32	0.53	−
RBPLJ0114+1325	−	01:14:52.8	+13:25:37.5	0.583*	Stadnik & Romani (2014)	3	v	59	4	4	7.04	0.48	0.74	−
RBPLJ0136+3905	B3 0133+388	01:36:32.5	+39:05:59.6	0.750	Neronov et al. (2015)	6	v	7	2	27	−	−	−	−
RBPLJ0136+4751	OC 457	01:36:58.6	+47:51:29.0	0.859	Hewitt & Burbidge (1987)	3	v	64	4	3	8.75	0.64	0.86	−
RBPLJ0152+0146	RBS 0248	01:52:39.6	+01:47:17.4	0.08	Laurent-Muehleisen et al. (1998)	6	4	9	2	20	−	−	−	−
RBPLJ0211+1051	−	02:11:13.2	+10:51:35.0	0.2*	Meissner & Romani (2010)	3	v	65	4	3	14.98	0.51	0.31	−30.0
RBPLJ0217+0837	−	02:17:17.1	+08:37:03.9	0.085	Shaw et al. (2013)	3	v	62	4	3	6.11	0.47	0.50	76.0
RBPLJ0221+3556	S4 0218+35	02:21:05.5	+35:56:13.9	0.944	Cohen et al. (2003)	5	v	1	1	−	−	−	−	−
RBPLJ0222+4302	3C 66A	02:22:39.6	+43:02:07.8	0.37	Furniss et al. (2013)	5,6	v	25	2	6	7.99	0.40	0.38	16.0
RBPLJ0232+2017	−	02:32:48.6	+20:17:17.4	0.14	Schachter et al. (1993)	6	4	8	2	18	−	−	−	−
RBPLJ0238+1636	AO 0235+164	02:38:38.9	+16:36:59.0	0.94	Hewitt & Burbidge (1987)	5	v	20	3	5	12.15	0.49	0.39	22.0
RBPLJ0259+0747	PKS 0256+075	02:59:27.1	+07:47:39.6	0.893	Murphy et al. (1993)	3	v	34	3	5	23.59	0.47	0.07	53.0
RBPLJ0303+4716	B3 0300+470	03:03:35.2	+47:16:16.3	0.475	Hughes et al. (1992)	5	v	15	3	10	7.25	0.45	0.40	81.0
RBPLJ0303–2407	PKS 0301–243	03:03:26.5	−24:07:11.5	0.2657	Pita et al. (2014)	3	v	12	3	17	6.67	0.24	0.19	54.0
RBPLJ0316+4119	TXS 0313+411	03:16:43.0	+41:19:29.9	0.01894	Bernardi et al. (2002)	5	4	8	2	19	−	−	−	−
RBPLJ0319+1845	RBS 0413	03:19:51.8	+18:45:34.4	0.19	Stocke et al. (1991)	5,6	v	7	3	12	−	−	−	−
...														

^a - Redshift notes: (*) non spectroscopic redshift, (l) lower limit on redshift, (m) multiple values are present in literature. ^b - Sample IDs: (1) γ -ray-loud sub-sample from the 'June survey' sample, (2) γ -ray-quiet sub-sample from the 'June survey' sample, (3) γ -ray-loud sub-sample from the monitoring sample, (4) γ -ray-quiet sub-sample from the monitoring sample, (5) additional sample of 68 hand-picked sources of high interest, (6) ISP/HSP blazar sample. ^c - fixed aperture is given in arcsec, 'v' denotes variable aperture (for details see sections 4.1.2 and 6).

Table A2. Monitoring data: (1) - J2000 name; (2) - Julian Date; (3,4) - Q/I, U/I relative Stokes parameters before the correction for the instrumental polarization; (5,6) - Q/I and U/I relative Stokes parameters corrected for the instrumental polarization and EVPA zero-point; (7,8) - Fractional polarization and polarization vector position angle corrected for the instrumental polarization and EVPA zero-point. This table gives only first 3 rows of the entire dataset, which can be accessed at <https://doi.org/10.7910/DVN/IMQKSE>.

AGN ID	JD	Q/I _{inst}	U/I _{inst}	Q/I	U/I	PD %	EVPA deg
(1)	(2)	(3)	(4)	(5)	(6)	(7)	(8)
RBPLJ0017+8135	2451023.41611	0.0131 ± 0.00022	0.0121 ± 0.00012	0.0131 ± 0.00022	0.0121 ± 0.00012	5.2 ± 0.3	20.4 ± 1.2
RBPLJ0017+8135	2459016.01214	0.0031 ± 0.00002	0.0048 ± 0.00005	0.0431 ± 0.00022	0.1221 ± 0.00022	12.2 ± 0.1	20.4 ± 1.2
RBPLJ0017+8135	2459086.08916	0.0536 ± 0.00003	0.0022 ± 0.00006	0.0321 ± 0.00022	0.0441 ± 0.00043	6.2 ± 0.2	120.4 ± 2.1
...							

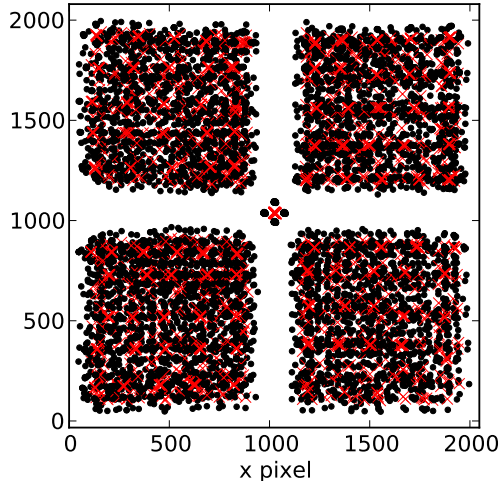


Figure B1. A plot showing the location of unpolarized standard stars used for the combined 2013 – 2017 instrument model. The individual spots are indicated by black dots, and the central point by a red cross.

APPENDIX B: INSTRUMENT MODEL

The instrument model accounts for two separate imperfections of the *RoboPol* polarimeter: the spatial distortions of the four spots pattern on the CCD, and the instrumental polarization across the FoV. The functional dependencies used for approximation of the instrument response are given in King et al. (2014). Here we present updated plots of the instrument model parameters obtained from 11 series of exposures of 7 standard unpolarized stars observed at different positions across the FoV in 2013 – 2017. The locations of these standard stars on the CCD are shown in B1.

Figures B2 - B4 demonstrate variation of parameters $\Delta_x(x, y)$, $\delta_x(x, y)$ and $\phi_x(x, y)$ of the spatial model depicted in Fig. 3 across the FoV. The y version of these parameters looks similar. The corresponding plots were omitted for brevity.

Figures B5 and B6 demonstrate effectiveness of the instrument intensity model used to correct the measured spot intensities for systematic variation of the instrumental polarization across the FoV. The distribution of the residual Q/I and U/I Stokes parameters of the unpolarized standards measured in the field after the instrumental polarization correction is shown in Fig. B7. For the detailed description of the instrument model correction we forward readers to King et al. (2014).

This paper has been typeset from a $\text{\TeX}/\text{\LaTeX}$ file prepared by the author.

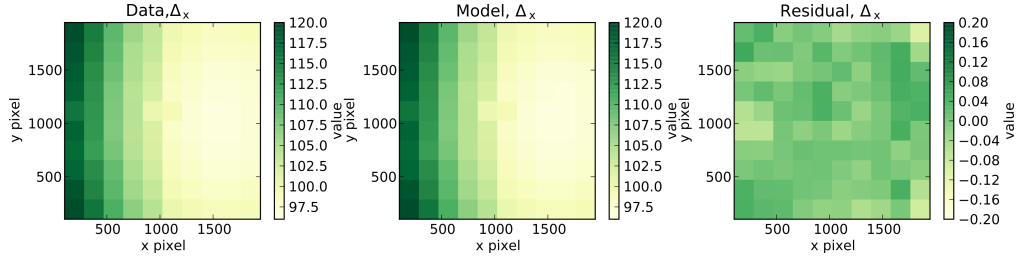


Figure B2. The data (left), best-fit model (centre), and residuals (right) for the quantity Δ_x in the instrument spatial pattern model. Note the change in colour scale for the residual plot.

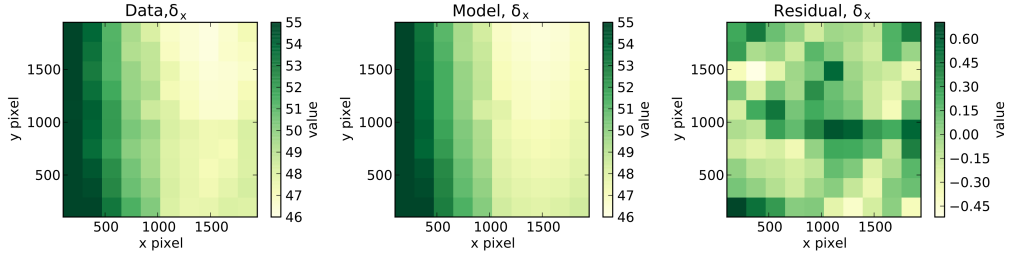


Figure B3. The data (left), best-fit model (centre), and residuals (right) for the quantity δ_x in the instrument spatial pattern model. Note the change in colour scale for the residual plot.

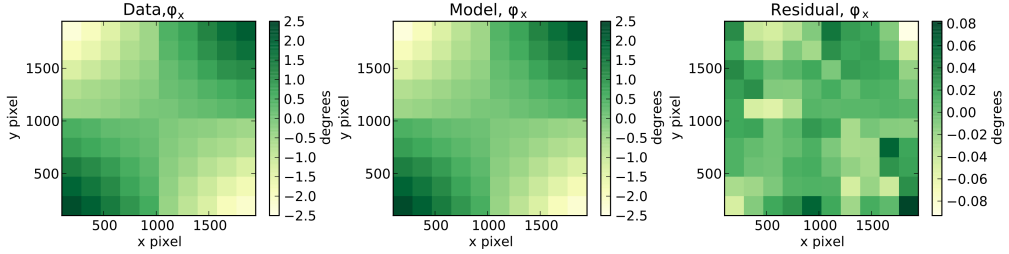


Figure B4. The data (left), best-fit model (centre), and residuals (right) for the quantity ϕ_x in the instrument spatial pattern model. Note the change in colour scale for the residual plot.

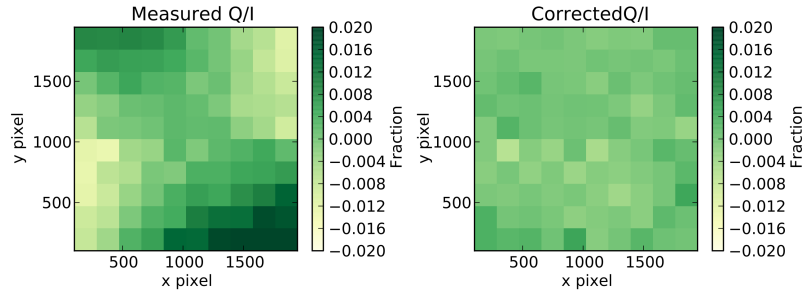


Figure B5. The uncorrected (left) and corrected (right) relative Stokes Q/I parameter, which corresponds to before and after applying the instrument intensity model to the data, respectively.

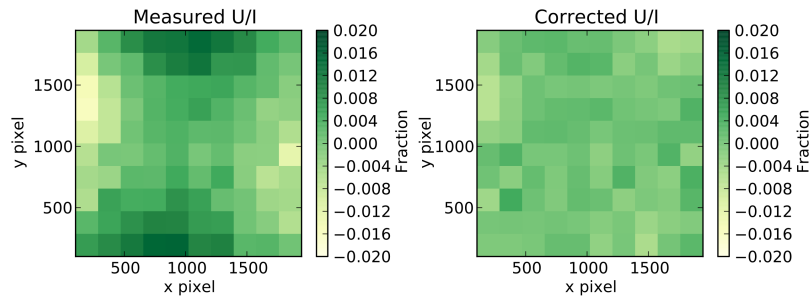


Figure B6. The uncorrected (left) and corrected (right) relative Stokes U/I parameter, which corresponds to before and after applying the instrument intensity model to the data, respectively.

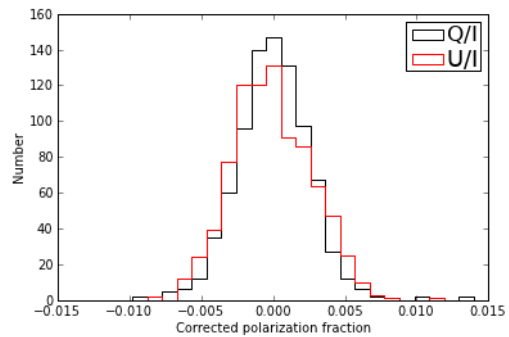


Figure B7. Residuals of relative Stokes parameters after the instrument model fit.